JOURNAL OF AIRCRAFT
Vol. 43, No. 3, May–June 2006

Poststall Prediction of Multiple-Lifting-Surface Configurations Using a Decambering Approach

Rinku Mukherjee* and Ashok Gopalarathnam†
North Carolina State University, Raleigh, North Carolina 27695-7910

A novel scheme, based on an iterative decambering approach, is presented for the prediction of poststall characteristics of wings using known section data as inputs. The scheme is suitable for implementation in lifting-line and vortex-lattice methods. The new scheme differs from earlier ones in the details of how the residual for the Newton iteration is computed. With earlier schemes, multiple solutions for wings at poststall conditions were identified only by observing that the final converged solution depended on the initial solution used for the iteration. With the current scheme, multiple solutions at poststall conditions are brought to light right during the computation of the residuals for the Newton iteration. In general, the new scheme is found to be more robust at achieving convergence. Validation is provided by comparison with experimental data in the literature and by showing the capability to predict well-known trends in stall behavior. The current method is also shown to have significant potential for providing valuable information for prediction of aircraft stability and control characteristics at poststall conditions.

Nomenclature

a_0	=	airfoil lift-curve slope in potential flow
C_L	=	wing lift coefficient
C_l	=	airfoil lift coefficient
C_m	=	airfoil pitching-moment coefficient about the quarter-chord
c	=	chord
D	=	damping factor
$\boldsymbol{F}$	=	residual vector
f	=	element of residual vector
i, j	=	index of wing section
$\boldsymbol{J}$	=	Jacobian matrix
N	=	number of wing sections
p	=	perturbation to δ_1 or δ_2
x_2	=	chordwise start location of the second decambering function
α	=	angle of attack
β	=	angle of yaw
Γ	=	strength of bound vortex
$\delta\boldsymbol{x}$	=	vector containing the corrections to the Newton variables
$\delta_1(x)$	=	first decambering function
$\delta_2(x)$	=	second decambering function
θ_2	=	angular coordinate corresponding to x_2

Subscripts

eff	=	effective
max	=	maximum
p	=	perturbed value (for a given step of the iteration)
s	=	starting value (for a given step of the iteration)
t	=	target value (for a given step of the iteration); also tail
visc	=	represents value from two-dimensional viscous experimental or computational data
w	=	wing
1	=	scheme 1
2	=	scheme 2

Received 23 December 2004; revision received 18 August 2005; accepted for publication 22 August 2005.

*Graduate Research Assistant, Box 7910, Department of Mechanical and Aerospace Engineering; currently Staff Scientist, MV Systems, Inc., 17301 W. Colfax, Avenue Suite 305, Golden, CO 80401; mvun75@yahoo.com. Member AIAA.

†Associate Professor, Box 7910, Department of Mechanical and Aerospace Engineering; ashok_g@ncsu.edu. Senior Member AIAA.

Introduction

THE ability of linear aerodynamic methods such as lifting-line theory (LLT), Weissinger's method, and vortex-lattice methods (VLM) to successfully predict the lift and induced drag behavior of medium- to high-aspect-ratio wings is well established. In these methods, a linear lift curve with a slope of approximately 2π per radian is typically assumed for the airfoil sections that form the wings. For several decades, researchers have sought to extend these linear prediction methods to handle the aerodynamic analysis of wings in which nonlinear airfoil lift curves are taken into consideration. The motivation behind these efforts was provided by the desire to predict stall and poststall aerodynamic characteristics of wings using experimental or computational section aerodynamic data for poststall conditions. It is recognized that the flow over a wing at poststall conditions is highly three dimensional, and the use of a quasi-two-dimensional approach represents a significant approximation. The impetus for such a prediction method, however, is provided by the need for rapid aerodynamic prediction capabilities for such high-alpha conditions for aircraft stability, control and simulation purposes and in the early phases of vehicle design. Furthermore, even high-order computational-fluid-dynamics (CFD) techniques are only now approaching the stage where they can be reliably used for high-alpha aerodynamic prediction. These CFD high-alpha analyses, however, require massive computing resources and significant time even for the analysis at a single angle of attack. Thus the search for rapid, albeit approximate, approaches for stall and poststall prediction of wings using known section data continues to be of interest.

The approaches for extending linear aerodynamic prediction methods to handle nonlinear and poststall airfoil lift curves can be broadly classified into two kinds: the iterative Γ-distribution approach and the α-correction approach. In the first approach, a lift distribution is first assumed on the wing and is then iteratively corrected by determining the effective-α distribution using the nonlinear airfoil lift curve. In the second approach, the deviation of the airfoil nonlinear lift curve from the potential-flow linear lift curve is used to apply a correction to the local α at each section of the wing. The following paragraphs provide brief descriptions of the two approaches.

Iterative Γ-Distribution Approach

Tani,[1] in 1934, is believed to have developed the first successful technique for handling nonlinear section lift curves in the LLT

formulation. In his technique, a spanwise bound vorticity Γ distribution is first assumed; this distribution is used to compute the distribution of induced velocities and hence induced angles α_i and effective angles of attack α_{eff} along the lifting line. The distribution of α_{eff} is then used to look up the operating C_l of the local section using the known nonlinear C_l-α data for the airfoil. A new Γ distribution is then computed from the spanwise C_l distribution. The iteration is carried out until the Γ distribution converges. This method worked well up to the onset of stall and was made popular by the 1947 NACA report of Sivells and Neely[2] that provided a detailed description of the method and implemented a tabular procedure for hand calculation of the method for unswept wings with arbitrary planform and airfoil lift-curve slopes. This method was applied for analysis of wings up to the onset of stall, that is, until a wing angle of attack at which some section on the wing has C_l equal to the local section $C_{l\max}$. At higher angles of attack where some sections on the wing might have a negative lift-curve slope, this successive-approximation approach appears to have failed.

Extensions of the approach to poststall angles of attack have been investigated in several subsequent research efforts. Based on a suggestion by von Kármán, Schairer[3] and Sears[4] investigated the possibility of nonunique solutions for poststall angles of attack. Their research showed that multiple solutions are possible for poststall angles of attack and include asymmetric lift distributions even when the flight condition and geometry are perfectly symmetrical. Subsequently, Piszkin and Levinsky[5] and Levinsky[6] developed a nonlinear lifting-line method based in part on the iterative approach originally conceived by Tani.[1] In addition to confirming the possibility of multiple solutions at poststall angles of attack, Piszkin and Levinsky also found that some of the converged solutions from their method exhibited sawtooth-type oscillations in the spanwise lift distributions. Because they were restricted to the use of 10 panels per side of the wing in their computer program, however, Piszkin and Levinsky were unable to determine whether or not the oscillations were a consequence of the coarse panel distribution. They presented the occurrence of lift hysteresis for increasing and decreasing α and the occurrence of zero-β rolling moments at poststall conditions. Their results confirmed that for a poststall angle of attack the final solution often depends on the starting solution for the initial lift distribution. In other words, multiple solutions are possible for the converged lift distribution for a poststall condition.

Anderson et al.[7] published a nonlinear lifting-line theory in 1980 that they applied to drooped leading-edge wings below and above stall. They presented results for wing C_L-α curves that extended to very high poststall angles of attack close to 50 deg. A similar approach was independently developed and presented by McCormick,[8] in which the nonlinear lifting-line theory was used to examine the loss in roll damping for a wing near stall. In both Refs. 7 and 8, it is reported that no asymmetric lift distributions for symmetric flight conditions were observed even when the iterations were started with asymmetric initial lift distributions. These observations are different from those of Sears and Levinsky.

α-Correction Approach

An entirely different approach to the use of nonlinear section data was developed by Tseng and Lan[9] in 1988. Although their primary focus was on vortex-dominated flows on low-aspect-ratio fighter-type wings at high α, they incorporated the effect of boundary-layer separation by iteratively reducing the angle of attack at each section of the wing. In their method, the α reduction at any given wing section is determined by the difference between the potential-flow C_l and the viscous C_l, with the latter being obtained from the nonlinear section C_l-α curve. In contrast to the iterative Γ-distribution approach, which can be used only in LLT-based methods because of the explicit use of the induced and effective angles of attack in the iteration, the α-reduction approach can be incorporated in LLT, Weissinger's method, and VLM. As a result, it can be used on swept, low-aspect-ratio wings, and multiple-wing configurations. More recently, the α-correction approach was used by van Dam et al.[10] for rapid estimation of $C_{L\max}$ and other high-lift characteristics for airplane configurations. In their work,[10] the authors show the effectiveness of using the α-correction approach for wing $C_{L\max}$ prediction with two-dimensional aerodynamic characteristics obtained using CFD computations with a Reynolds-averaged Navier–Stokes code. Additionally, the results of Ref. 10 also demonstrate how the α-correction approach is successful in estimating the $C_{L\max}$ of wings with part-span flaps, particularly when the start of the trailing-vortex wake over the flapped portion is displaced vertically to account for the downward location of the flap trailing edge.

In the current research, a decambering approach has been developed for predicting poststall aerodynamic characteristics of wings using known section data. In this approach, the chordwise camber distribution at each section of the wing is reduced to account for the viscous effects at high angles of attack. This approach is similar in concept to the α-correction approach[9,10] and can be incorporated in LLT, Weissinger's method, and VLM. It differs from the α-correction approach in its capability to use both the C_l and C_m data for the section and in the use of a two-variable function for the decambering. Also, unlike all of the earlier methods, the current approach uses a multidimensional Newton iteration that accounts for the cross-coupling effects between the sections in predicting the decambering for each step in the iteration. In addition, a novel scheme has been developed for computing the residuals for the iteration that brings to light multiple solutions at poststall conditions right during the iteration process itself rather than as a consequence of using multiple starting solutions. The following section illustrates the concept of decambering using an example two-dimensional flow past an airfoil. The iterative approach for three-dimensional wings is discussed next. Results for single and multiple wings are then presented.

Illustration of the Decambering Concept

This section provides an illustration of the decambering approach and demonstrates the concept by using a simple example of a two-dimensional flow past an NACA 0012 airfoil. It is illustrative to examine this approach for the two-dimensional situation first because the approach as applied to the flow past a three-dimensional finite wing will be described in the following section.

With increasing angle of attack, the boundary layer on the upper surface of an airfoil thickens and finally separates. It is this flow separation that causes the viscous C_l and C_m to deviate from the potential-flow theory predictions. These deviations can be related to the effective change in the chordwise camber distribution because of the boundary-layer displacement thickness and separation. If the effective decambering is taken into account, then a potential-flow prediction for the decambered airfoil will closely match the viscous C_l and C_m for the high-α flow past the original airfoil shape. This decambering idea served as the basis for the formulation of the current approach for the three-dimensional flow problem.

Although the camber reduction caused by the boundary layer on an airfoil can be determined from computational analyses, no such detailed information is available from wind-tunnel results. Wind-tunnel results for airfoils typically consist of only the C_l-α and C_m-α curves. This section discusses the approach for determining an "equivalent" camber reduction from the C_l-α and C_m-α data for an airfoil. More specifically, the effective decambering for a particular α is computed using the deviations of the viscous C_l and C_m from the potential-flow predictions for that airfoil. These deviations in C_l and C_m are denoted by ΔC_l and ΔC_m, respectively.

In the current method, the effective decambering of an airfoil is approximated using a function of two variables δ_1 and δ_2, as shown in Fig. 1. These two linear functions are added to obtain the final decambering function. The reason for using two variables is that the decambering is determined from two pieces of information: the C_l and the C_m for the α under consideration. Of course, this approximation will not match the actual viscous decambering, but the objective here is only to find an equivalent camber reduction in order to match the viscous C_l and C_m for the α under consideration.

The incremental effects of δ_1 and δ_2 on the changes to C_l and C_m for a given α can be computed reasonably well using thin airfoil theory and a three-term Fourier series approximation for a flat plate with a flap deflection.[11] For any given α, ΔC_l and ΔC_m are

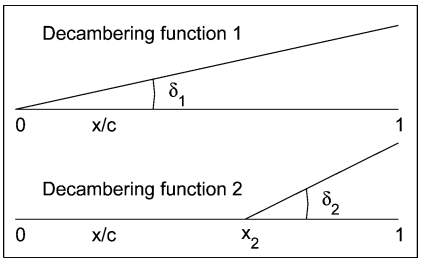

Fig. 1 Schematic diagram of decambering functions 1 and 2 (δ_1 and δ_2 are negative as shown and exaggerated for clarity).

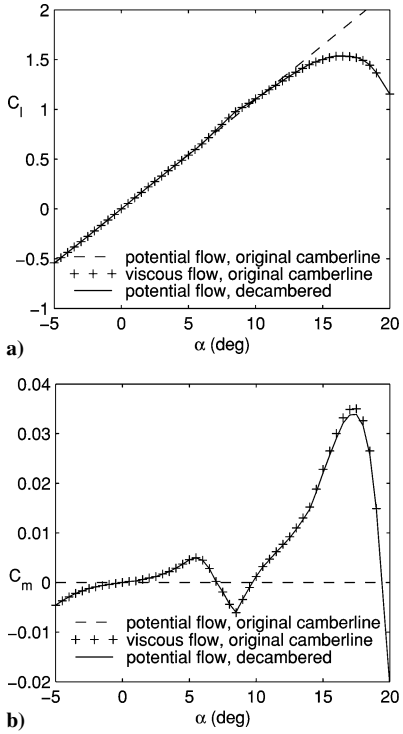

Fig. 2 Comparison of potential-flow predictions for the decambered airfoil with the viscous-flow values for the original airfoil: a) C_l and b) C_m.

defined as the differences between the viscous and the potential-flow predictions for C_l and C_m as follows:

$$\Delta C_l = (C_l)_{\text{viscous}} - (C_l)_{\text{potential}} \tag{1}$$

$$\Delta C_m = (C_m)_{\text{viscous}} - (C_m)_{\text{potential}} \tag{2}$$

If ΔC_l and ΔC_m are known for a given α, then the values of δ_1 and δ_2 in radians can be written as

$$\delta_2 = \frac{\Delta C_m}{\frac{1}{4}\sin 2\theta_2 - \frac{1}{2}\sin\theta_2} \tag{3}$$

$$\delta_1 = \frac{\Delta C_l - [2(\pi - \theta_2) + 2\sin\theta_2]\delta_2}{2\pi} \tag{4}$$

where θ_2 is the angular location in radians of the start point for the decambering function 2 shown in Fig. 1 and can be expressed in terms of its x/c location x_2 as follows:

$$\theta_2 = \cos^{-1}(1 - 2x_2), \qquad x_2 = 0.8 \tag{5}$$

In the current work, x_2 is arbitrarily assumed to be 0.8, although typically any value from 0.5 to 0.9 works well.

Thus, if the potential-flow and viscous-flow C_l-α and C_m-α data for an airfoil are available, the decambering function defined by δ_1 and δ_2 at each α can be determined. The effectiveness of the decambering approach is shown in Fig. 2 for an NACA 0012 airfoil. It can be seen from Fig. 2 that the potential-flow C_l-α and C_m-α predictions for the decambered airfoil closely match the corresponding viscous data, demonstrating that the two-variable decambering function is appropriate for the current objective. In this comparison, the viscous results were computed using the XFOIL[12] code, and the potential-flow results for the original and the decambered shapes were computed using a lumped-vortex method for thin camberlines.[11] The C_l predictions from the lumped-vortex method were corrected for thickness effects using an empirical approach[11] in which the C_l values were scaled by a factor of $[1 + 0.77(t/c)_{\max}]$.

In the following section, this decambering approach is extended to the analysis of multiple lifting surfaces, and the decambering at each wing section is evaluated in an iterative fashion.

Methodology

The objective of the research was to incorporate the two-variable decambering function in a three-dimensional analysis method such as a VLM in an iterative fashion. In a typical VLM, the lifting surface is divided into several spanwise and chordwise lattices. Associated with each lattice is a horseshoe vortex. Each spanwise section j (composed of a row of chordwise lattices) has two variables $\delta_{1\,j}$ and $\delta_{2\,j}$ for defining the local decambered geometry at that section.

Unlike in the two-dimensional illustration, where the δ_1 and δ_2 were selected to match the differences between the potential-flow and the viscous-flow results, in the three-dimensional case, changing a δ on one section is likely to have a significant effect on the neighboring sections and on the sections of the downstream lifting surfaces. To account for these effects, a $2N$-dimensional Newton iteration is used to predict the δ_1 and δ_2 at each of the N sections of all of the wings so that the ΔC_l and ΔC_m at these sections approach zero as the iteration progresses. A $2N \times 2N$ matrix equation, as shown in Eq. (6) is solved at each step of the Newton iteration.[13]

$$\boldsymbol{J} \cdot \delta\boldsymbol{x} = -\boldsymbol{F} \tag{6}$$

In this equation, $\boldsymbol{F}$ is a $2N$-dimensional vector containing the residuals of the functions f_i to be zeroed, $\delta\boldsymbol{x}$ is the $2N$-dimensional vector containing the corrections required to the $2N$ variables x_i to bring the elements of vector $\boldsymbol{F}$ closer to zero, and $\boldsymbol{J}$ is the $2N \times 2N$ Jacobian of the system containing the gradient information.

The Jacobian is partitioned into four submatrices as shown in Eq. (7). Equations (8–11) show the elements of the four submatrices to illustrate the computation of the changes to ΔC_l and ΔC_m at section i as a result of small perturbations to the decambering variables δ_1 and δ_2 at section j.

$$J = \begin{pmatrix} J_{l1} & J_{l2} \\ J_{m1} & J_{m2} \end{pmatrix} \tag{7}$$

$$(J_{l1})_{i,j} = \frac{\partial \Delta C_{li}}{\partial \delta_{1,j}} = \frac{\left(C_{l\,p}\right)_i - \left(C_{l_s}\right)_i}{\left[\left(\delta_{1s}\right)_j + p\right] - \left(\delta_{1s}\right)_j} \tag{8}$$

$$(J_{m1})_{i,j} = \frac{\partial \Delta C_{mi}}{\partial \delta_{1,j}} = \frac{\left(C_{m\,p}\right)_i - \left(C_{m_s}\right)_i}{\left[\left(\delta_{1s}\right)_j + p\right] - \left(\delta_{1s}\right)_j} \tag{9}$$

$$(J_{l2})_{i,j} = \frac{\partial \Delta C_{li}}{\partial \delta_{2,j}} = \frac{\left(C_{l\,p}\right)_i - \left(C_{l_s}\right)_i}{\left[\left(\delta_{2s}\right)_j + p\right] - \left(\delta_{2s}\right)_j} \tag{10}$$

$$(J_{m2})_{i,j} = \frac{\partial \Delta C_{mi}}{\partial \delta_{2,j}} = \frac{\left(C_{m\,p}\right)_i - \left(C_{m_s}\right)_i}{\left[\left(\delta_{2s}\right)_j + p\right] - \left(\delta_{2s}\right)_j} \tag{11}$$

For each step of the iteration, $\boldsymbol{F}$ and $\boldsymbol{J}$ are determined, and $\delta\boldsymbol{x}$ is computed using Eq. (6). The corrections are then applied to the values of δ_1 and δ_2 for all of the sections in an effort to bring the residuals closer to zero. Using this overall methodology, two schemes have been formulated for determining the poststall solution of a finite wing. The two schemes differ in the details of how the residuals

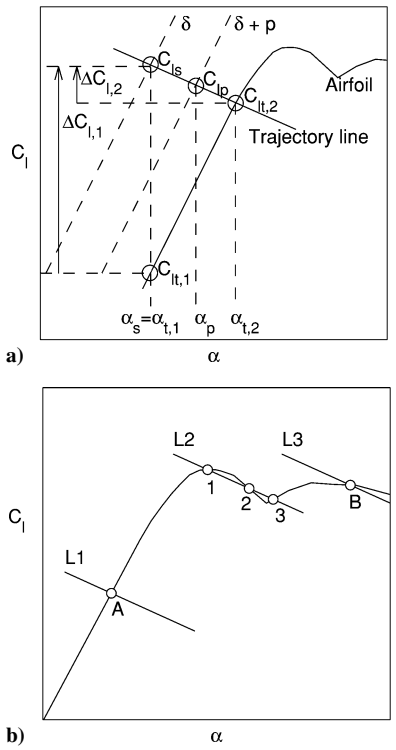

Fig. 3 Residual computation: a) illustration of the differences in computation of the residuals using schemes 1 and 2 and b) illustration of the different ways in which trajectory lines for scheme 2 can intersect the airfoil C_l-α curve.

are computed. The first scheme, introduced in Ref. 14, was found to work well for certain airfoil lift curves, but failed to converge for several other lift-curve shapes. This lack of robustness provided the impetus for developing the second scheme. These two schemes have been incorporated in a custom vortex-lattice method VLM3D and in a discrete-vortex Weissinger's method code WINGS. All of the results in this paper are from the VLM3D code.

The iteration procedure and the two schemes can be summarized using the following steps and Fig. 3a:

1) Assume starting values of the decambering variables δ_1 and δ_2 for each section of each wing; for example, section j has starting values denoted by $(\delta_{1_s})_j$ and $(\delta_{2_s})_j$.

2) Compute, using VLM3D, the aerodynamic characteristics of the lifting-surface configuration, each section of which has been decambered by δ_{1_s} and δ_{2_s} for that section. VLM3D accounts for the decambering by appropriately rotating the unit normal vector of each lattice. The VLM3D analysis provides the C_l and C_m of each section as output. These are the starting values for the current step of the iteration and are denoted by $(C_{l_s})_j$ and $(C_{m_s})_j$ for section j. $(C_{l_s})_j$ is shown in Fig. 3a.

3) Compute the starting values of the effective angle of attack of each section, denoted by α_s in Fig. 3a, corresponding to the section C_l; for example, the effective angle of attack of section j is denoted by $(\alpha_s)_j$ and is obtained by setting $(C_l)_{\text{sec}} = (C_{l_s})_j$ in the following equation:

$$\alpha_{\text{eff}} = (C_l)_{\text{sec}}/a_0 - \delta_1 - \delta_2(1 - \theta_2/\pi + \sin\theta_2/\pi) + \alpha_{0l} \qquad (12)$$

which describes the relationship between the local C_l and local α for a decambered section operating in potential flow with a section lift-curve slope of a_0 (typically 2π per radian), zero-lift angle of attack of α_{0l} for the original section without decambering, and decambering variables of δ_1 and δ_2. In Eq. (12), the last three terms together represent the zero-lift angle of attack of the decambered section.

4) *Residuals for scheme 1:* Compute the target C_l for each section as the C_l on the airfoil C_l-α curve corresponding to $(\alpha_s)_j$; for example, the target C_l of section j is given by $(C_{l_{t,1}})_j$ (subscript 1 denotes scheme 1), as shown in Fig. 3a. Similarly, $(C_{m_{t,1}})_j$, the target C_m for section j, is the C_m on the airfoil C_m-α curve corresponding to $(\alpha_s)_j$. Hence, compute the residuals for scheme 1 as $\Delta C_{l,1} = (C_{l_s})_j - (C_{l_{t,1}})_j$ and $\Delta C_{m,1} = (C_{m_s})_j - (C_{m_{t,1}})_j$.

5) Perturb δ_1 at section j by adding a small perturbation p.

6) Compute the wing aerodynamic characteristics with the perturbed decambering using VLM3D; the resulting C_l and C_m for section j are denoted by $(C_{l_p})_j$ and $(C_{m_p})_j$. $(C_{l_p})_j$ is shown in Fig. 3a. Hence, compute the jth column of J_{l1} and J_{m1} using Eqs. (8) and (9).

7) *Residuals for Scheme 2:* Compute the effective angle of attack of each section for the perturbed decambering, denoted in Fig. 3a by α_p; for example, the effective angle of attack of section j is obtained by setting $(C_{l\text{sec}}) = (C_{l_p})_j$ in Eq. (12). This effective angle of attack is denoted by $(\alpha_p)_j$ for section j. The line joining the points $[\alpha_s, C_{l_s}]$ and $[\alpha_p, C_{l_p}]$ for any section is called the "trajectory line" for that section, as it determines the linearized trajectory of how a point on the C_l-α curve defined by the section α_{eff} and section C_l moves with changes to δ_1 on that section. This trajectory line is illustrated in Fig. 3a. Therefore, in scheme 2, the target C_l, $(C_{l_{t,2}})_j$, of section j for example, is the point of intersection between the trajectory line for section j and the airfoil lift curve for the section as illustrated in Fig. 3a. The corresponding α is $(\alpha_{t,2})_j$, which is the α of the point of intersection. The target pitching-moment coefficient, $(C_{m_{t,2}})_j$ is C_m on the airfoil C_m-α curve corresponding to $(\alpha_{t,2})_j$. The residuals for scheme 2 are now computed as $(\Delta C_{l,2})_j = (C_{l_s})_j - (C_{l_{t,2}})_j$ and $(\Delta C_{m,2})_j = (C_{m_s})_j - (C_{m_{t,1}})_j$.

8) Reset the value of δ_1 at section j to $(\delta_{1_s})_j$.

9) Cycle through steps 5–8 for all values of the section index j to compute all of the columns of J_{l1} and J_{m1}.

10) Repeat steps 5–9 now perturbing δ_2 instead of δ_1 to compute J_{l2} and J_{m2}. In this process, the computation of the residuals for scheme 2 in step 7 is ignored, as they have already been computed.

11) Using the Newton equation in Eq. (6), compute the correction vector $\delta\boldsymbol{x}$. Update the values of δ_{1_s} and δ_{2_s} by adding the correction vector $\delta\boldsymbol{x}$ multiplied by a user-specified damping factor D (also referred to under-relaxation factor), and go to step 2.

This iteration process is carried out until all of the residuals have converged to a specified tolerance. In the current work a damping factor of 0.1 and a tolerance of 0.001 have been used in all of the examples.

Multiple intersections with Inclined Trajectory Line

Figure 3b illustrates an important consequence of using an inclined trajectory line for determining the target C_l in scheme 2. Three possible ways in which the trajectory line can intersect the airfoil lift curve are illustrated in Fig. 3b: 1) the trajectory line marked as L1 intersects the airfoil lift curve at a single prestall point, 2) the trajectory line marked as L2 intersects the airfoil lift curve at multiple points, and 3) the trajectory line marked as L3 intersects the airfoil lift curve at a single point in the poststall region. Although there is no ambiguity in determining the values of the target C_l for lines L1 and L3, there clearly are three possible choices for the target C_l for line L2. This illustration clearly demonstrates that it is possible to obtain multiple solutions for poststall conditions, a fact that was apparently first suggested by von Kármán (see Ref. 4) and has since been discussed by several researchers.[3–8,14] However, the approach in scheme 2 is novel because this scheme is believed to be the first one in which the possibility of multiple solutions for high angles of attack is brought to light right during the iteration process. Earlier approaches including scheme 1 were able to identify the existence of multiple solutions only as a result of obtaining multiple final converged solutions with different initial conditions for the iteration procedure.

The existence of multiple intersections also presents a dilemma in choosing an appropriate target C_l from the possible multiple solutions. The following procedure was developed for making the choice during the iteration process. At each step of the iteration, each of the sections on all of the wings is examined to identify those with single intersections, as identified by points A and B in Fig. 3b. The target C_l values for these sections are identified without ambiguity. Using a logical switch called "lpoststall" in the code, each of these sections

is also tagged as "stalled" or "unstalled" depending on whether the α for the intersection point is greater than or less than the α for $C_{l\max}$. For example, lpoststall is tagged unstalled for point A and stalled for point B in Fig. 3b. The sections with multiple intersections are then examined. Using the trajectory line L2 in Fig. 3b for example, the intersection point 1 is chosen if the logical switch lpoststall for the section is unstalled, and the intersection point 3 is chosen if the logical switch for the section is stalled.

Next, another logic is applied in which all of the sections of the wings are scanned to identify sets of contiguous sections, all of which have multiple intersections and all of which are also tagged as unstalled. If any of these sets of contiguous sections are bound on both sides by sections tagged as stalled, then all of the sections in this set are switched to stalled. This logic largely removed any occurrence of unstalled regions with multiple intersections sandwiched between two stalled regions.

The values of the logical switch for all of the sections are carried over from one iteration to the next as well as from one α to the next when performing the analysis for a sequence of angles of attack. Thus, if a section gets tagged as stalled at any point in the iteration it remains tagged as stalled unless the section ends up with a trajectory line like L1 in Fig. 3b when it gets switched to unstalled.

Although the methodology uses a two-variable decambering function, for cases where the experimental or computational viscous data for the airfoil section does not have C_m information, or for cases where the decambering approach is applied to an analysis method that cannot compute the section pitching moments (e.g., LLT or a Weissinger's method), the decambering is modeled as a function of a single variable δ_1; δ_2 is set to zero. In this case, the viscous decambering function becomes similar to that used in the α-reduction approach.[9,10] The inclined trajectory line for computing the residuals in scheme 2 is still applicable when the single-variable decambering function is used, and this approach makes the scheme 2 different from those developed earlier.

Results

The iterative decambering approach has been implemented for the analysis of multiple-lifting-surface configurations in VLM3D, a custom VLM code. In this section, poststall results from VLM3D are presented for two airfoil lift curves, different planform shapes, and a wing-tail configuration. The computation of the residuals has been implemented using the two schemes, and the effectiveness of the two schemes is compared. The examples presented in this section are as follows:

1) In the first example, the results from the current method are compared with experimental results from the wind-tunnel tests by Ostowari and Naik.[15] In their work,[15] experimental C_l-α data for the NACA 4415 airfoil at a Reynolds number of 0.5×10^6 is presented along with experimental C_L-α data for constant-chord finite wings of several aspect ratios with the same airfoil and at the same Reynolds number. The airfoil and finite-wing data in Ref. 15 were obtained in the same wind tunnel. In this example, the two-dimensional experimental data have been used as input to the method, and the predicted finite-wing lift curves have been compared with the corresponding experimental data. This example has been used to compare the effectiveness of the two schemes and to illustrate how the converged solutions at poststall angles of attack are dependent on the starting solution used for the iteration.

2) The second example is used to study the effect of wing taper ratio on the stall characteristics of a wing and, in particular, how the stall progresses along the span with increasing angle of attack.

3) The third example, a wing-tail configuration is analyzed to demonstrate the capability of the current method to handle multiple-lifting-surface configurations. The effect of the wing stall on the aircraft pitching moment is shown to illustrate how the method can be used for providing information for the study of stability and control characteristics.

Example 1: Experimental Validation

In this example, experimental two-dimensional data[15] for an NACA 4415 airfoil at a Reynolds number of 0.5×10^6, shown in Fig. 4, is used as input to the VLM3D code to generate poststall results for an unswept rectangular wing of aspect ratio 12. The computational results for the wing of aspect ratio 12 are then compared with the corresponding experimental C_L-α curve from Ref. 15. Figure 5 shows the wing C_L-α curves from VLM3D using schemes 1 and 2. In the same figure, the airfoil C_l-α curve and the wing C_L-α curve from experiment[15] are also shown for comparison. In both schemes, the starting values of δ_1 and δ_2 for each α were taken from the converged values for the previous α. For the first α of the sequence, δ_1 was set to -40 deg and δ_2 was set to 0 deg for both schemes.

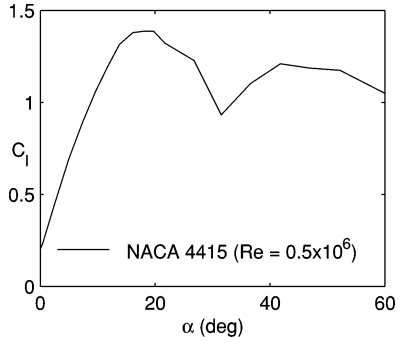

Fig. 4 Airfoil C_l-α curve used in example 1.

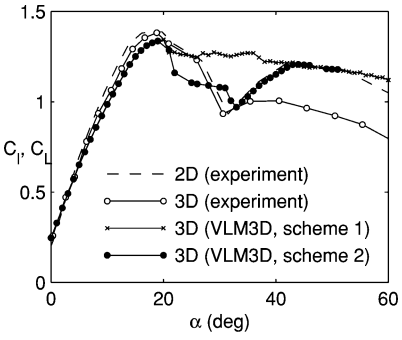

Fig. 5 Wing C_L-α predicted using the current method (VLM3D) for a rectangular wing of aspect ratio 12 and compared with experimental results from Ref. 15.

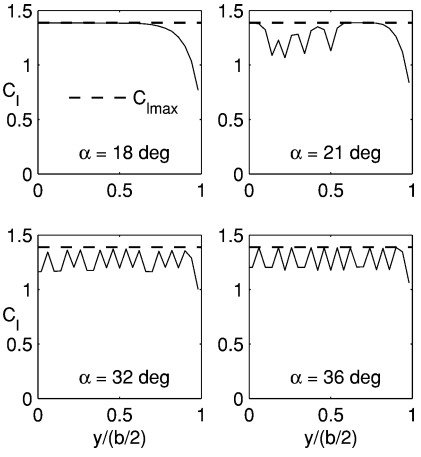

Fig. 6 Spanwise C_l distribution predicted for a rectangular wing of aspect ratio 12 using scheme 1.

As seen from Fig. 5, the predictions for the values of wing C_L at prestall angles of attack from the two schemes are identical. For poststall conditions, the results of scheme 2 are closer than those of scheme 1 to the experimental results. Figures 6 and 7 show the spanwise C_l distributions from the current method for angles of attack 18, 21, 32, and 36 deg from schemes 1 and 2, respectively.

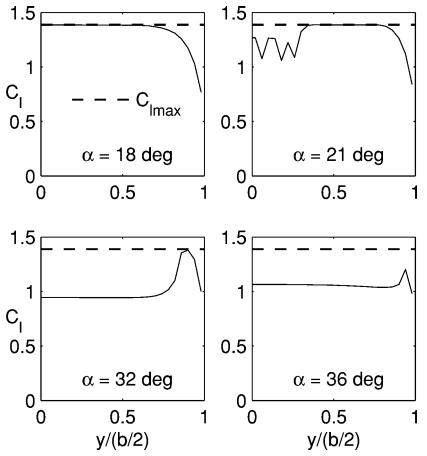

Fig. 7 Spanwise C_l distribution predicted for a rectangular wing of aspect ratio 12 using scheme 2.

For all of the results presented in Figs. 6 and 7, convergence was achieved to within a tolerance of 0.001 in ΔC_l and ΔC_m. $C_{L\max}$ occurs at around α of 18 deg. Experimental results for the spanwise C_l distributions were not available for comparison. As seen from the results of scheme 1 in Fig. 6, there is substantial "sawtooth behavior" in the spanwise C_l distributions with regions of unstalled flow sandwiched between regions of stalled flow. Such undesirable spanwise sawtooth oscillations are a common problem in numerical techniques that use known section data for the prediction of wing poststall characteristics, as also noted by other researchers.[6–8] Although these sawtooth results correspond to numerically converged solutions, it is believed that a real flow cannot have such spanwise oscillations. The results from scheme 2, shown in Fig. 7, do not exhibit these sawtooth oscillations for a majority of the conditions. For this reason, scheme 2 is considered more acceptable.

The wing C_L from scheme 2 in Fig. 5 shows that as the α is increased to 18 deg the C_L continues to increase. At this condition the entire wing remains unstalled as the section C_l values are less than the $C_{l\max}$ of 1.39. This can be confirmed by examining the spanwise section C_l distribution from scheme 2 in Fig. 7 for α of 18 deg. At 18 deg the inboard portion of the wing is close to stall. As the α is increased between 18 and 21 deg, the inboard portion of the wing stalls and a portion of the semispan between the root and the tip is close to stall, as can be seen from the spanwise section C_l distribution for α of 21 deg in Fig. 7. As the α is increased beyond 21 deg, the spanwise extent of the stalled portion increases. At 32 deg, most of the wing has stalled, and the outboard portion is close to stall, as shown in Fig. 7. Between 32 and 44 deg, the C_l on the stalled portion of the wing increases, as seen in Fig. 7 for α of 36 deg. The wing C_L therefore increases between 32 and 44 deg, as shown in Fig. 5. Beyond 44 deg, the wing C_L remains almost constant at 1.2.

As shown in Fig. 7, for α of 21 deg, oscillations are seen in the spanwise C_l distribution over the stalled portion of the wing. This sawtooth region at α of 21 deg is examined closely in Fig. 8a, and it illustrates that the sawtooth behavior occurs because of unstalled sections being sandwiched between stalled sections. Such oscillations were observed for a few angles of attack, even though the solutions are fully converged. Figure 8b shows the section C_l plotted against the section effective angle of attack on the airfoil C_l-α curve for the points corresponding to the upper and lower corners of the sawtooth region in Fig. 8a. It is seen that the upper corners of the sawtooth region (marked by $*$ in Figs. 8a and 8b) have converged to the unstalled region of the airfoil C_l-α curve as shown in Fig. 8b. The lower corners (marked by o in Figs. 8a and 8b), on the other hand, have converged to the stalled region of the airfoil C_l-α curve as shown in Fig. 8b. Because of the fact that the trajectory lines for the upper-corner points intersect the airfoil C_l-α curve at only a single point, the poststall logic was unable to remove such oscillations.

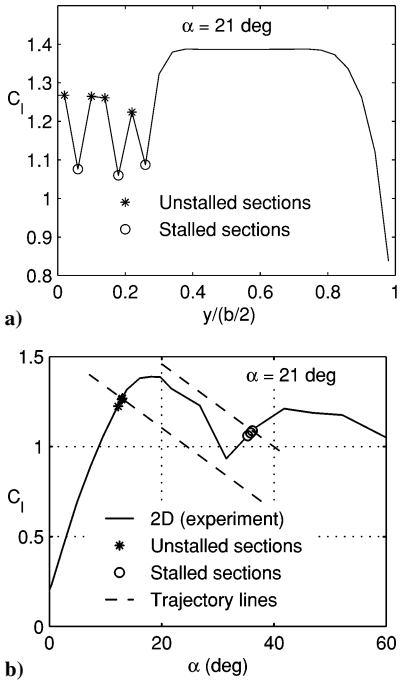

Fig. 8 Sawtooth behavior in the spanwise C_l distribution for a rectangular wing of aspect ratio 12: a) upper and lower corners of the sawtooth region and b) location of the upper and lower corners shown in Fig. 8a on the airfoil C_l-α curve.

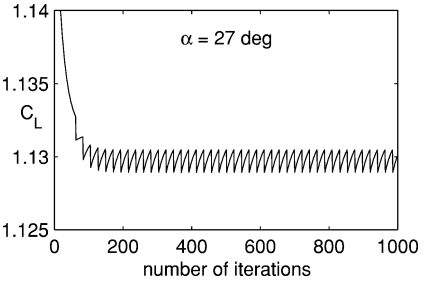

Fig. 9 Wing C_L variation with number of iterations for a rectangular wing of aspect ratio 12.

The predicted C_L-α results using scheme 2 in Fig. 5 are from an analysis for a sequence of angles of attack from -5 to 60 deg. In this angle-of-attack range, convergence was not achieved for a few angles of attack. The data points plotted in Fig. 5 are for only those angles of attack at which convergence was successfully achieved. For example, convergence was not achieved at α of 27 deg. Figure 9 shows the convergence plot for the wing C_L for α of 27 deg. It is seen that the wing C_L exhibits an undamped periodic oscillation with a small amplitude of approximately 0.001 in C_L and does not converge to any particular value.

For a majority of the cases, scheme 2 is successful in converging to realistic solutions. It is only for a few conditions that the converged solution has a sawtooth behavior (e.g., $\alpha = 21$ deg in Fig. 7) or the solution does not converge as a result of an undamped periodic convergence pattern as shown in Fig. 9.

Example 1: Effect of Initial Conditions for Scheme 2

Figure 10a shows the wing C_L-α predicted using scheme 2 for two different starting conditions for the Newton iteration: 1) $\delta_1 = -40$ deg for all sections at each α and 2) $\delta_1 = 0$ deg for all sections at each α. Figure 10b shows the spanwise C_l distributions for the two cases for α of 18 deg. The results clearly illustrate that multiple solutions are possible for poststall conditions. When the starting condition of $\delta_1 = 0$ deg is used, the starting solution corresponds to a stalled wing. As a result, for the portions of the wing that are stalled, the lpoststall logical switch gets tagged as stalled

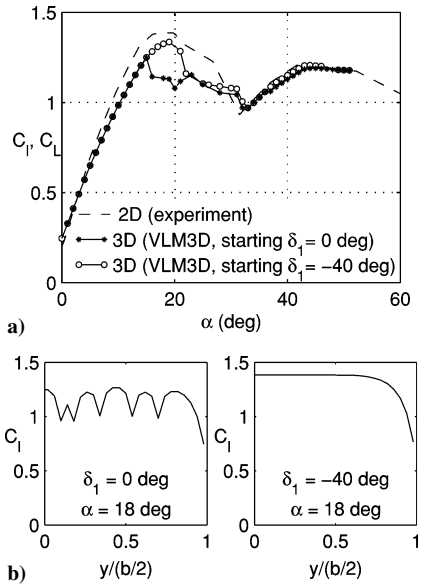

Fig. 10 Aerodynamic properties predicted for a rectangular wing of aspect ratio 12 for different starting values of δ_1 (the δ values shown were used to start the iteration at each alpha): a) wing C_L-α and b) spanwise section C_l.

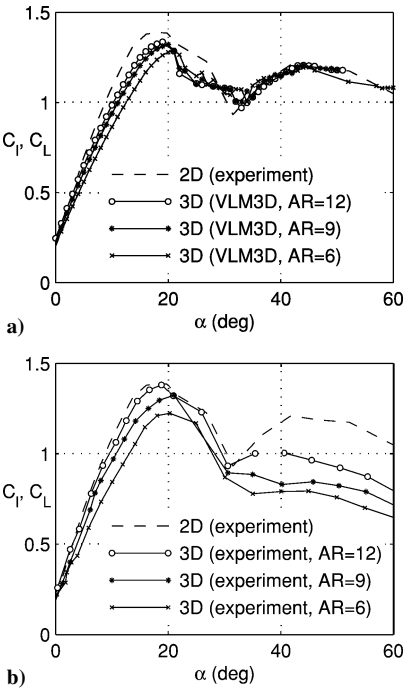

Fig. 11 Wing C_L-α for rectangular wings of aspect ratios 12, 9, and 6: a) predicted using the VLM3D code and b) from the wind-tunnel experiments of Ostowari and Naik.[15]

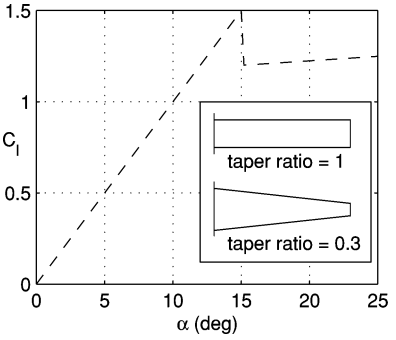

Fig. 12 Hypothetical airfoil lift curve used in examples 2 and 3, with inset showing right-side planform shapes of the wings used in example 2.

after the first iteration. On the other hand, when $\delta_1 = -40$ deg is used as the starting condition the starting solution corresponds to a completely unstalled wing even for a high angle of attack. As a result, the lpoststall gets tagged as unstalled after the first iteration. Thus the two different C_L-α curves for the two different starting values of δ_1, in effect, produce the hysteresis behavior that is similar to those often seen in experimental (see Refs. 6 and 7) and computational[6–8] results for increasing-α and decreasing-α sweeps. These results confirm the possibility of multiple solutions at poststall angles of attack pointed out by other researchers[3–8] and the sensitivity of poststall solutions not only to the initial conditions but also to the schemes used for the Newton iteration.

Example 1: Effect of Change to Aspect Ratio

In this section, the change to the predicted wing C_L-α curve with aspect ratio is studied using VLM3D. Three unswept rectangular wings of aspect ratios of 12, 9, and 6 have been used. Figure 11a shows the C_L-α curves of the three wings from VLM3D using scheme 2. In the same figure the airfoil C_l-α curve from experiment[15] is also shown for comparison. Figure 11b shows the results for the three wings from the experimental data of Ostowari and Naik.[15] It is seen that the current approach is successful in capturing all of the important trends.

Summary of Example 1

The results from schemes 1 and 2 in this example show that scheme 2 is more robust. The spanwise C_l distributions predicted using scheme 1 exhibit substantial undesirable sawtooth behavior. The spanwise C_l distributions predicted using scheme 2, on the other hand, are devoid of such oscillations for most of the angles of attack. Scheme 1 also has far more convergence problems than scheme 2. Scheme 2 is therefore found to be better suited for poststall prediction purposes, and the results presented henceforth will only be from scheme 2.

Example 2: Study of Stall Characteristics

In this example, the change to the stall characteristics with change to the wing taper ratio is studied using scheme 2. The airfoil used has a hypothetical lift curve as shown in Fig. 12. This lift curve is similar to those used by Sears[4] and by Levinsky.[6] Two unswept wings of aspect ratio 10 and taper ratios of 0.3 and 1.0 are studied. The right-side planforms of the wings are shown in the inset in Fig. 12.

The predicted wing C_L-α curves for the two wings are shown in Fig. 13, and the spanwise C_l distributions for α of 10, 17, 18, and 24 deg are shown in Fig. 14. It is observed from the wing C_L-α curves that the wing C_L increases as the α is increased to 16 deg. At these prestall conditions, the rectangular wing has the largest section C_l among the two wings for any given α, as seen from the spanwise C_l distributions for $\alpha = 10$ deg in Fig. 14. As a result, the rectangular wing is the earliest to stall and starts stalling from the root at $\alpha = 17$ deg. As seen from Fig. 14, the tapered wing, on the other hand, is not stalled at $\alpha = 17$ deg. At this α, although the root portion of the rectangular wing is stalled, the remainder of the wing is still well removed from stall in comparison to the tapered wing.

When α is increased to 18 deg, the tapered wing also stalls, with the stalled region extending more towards the wing tips than for the rectangular wing. As seen from Fig. 14, the spanwise extent of stall for the rectangular wing is largely unchanged between $\alpha = 17$ and 18 deg. For this reason, although the rectangular wing is the first to stall it has a gentler stall behavior than the tapered wing, as can be confirmed by an examination of the C_L-α curves in Fig. 13. For α greater than 18 deg, both the wings are significantly stalled.

These predictions of the gentle stall characteristics of a rectangular wing and the more abrupt tip-stall characteristics of the highly

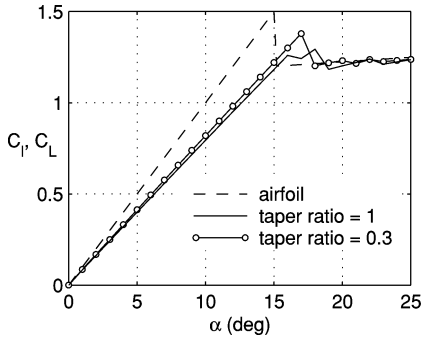

Fig. 13 Wing C_L-α curves for the rectangular and tapered wings used in example 2, predicted using VLM3D (scheme 2).

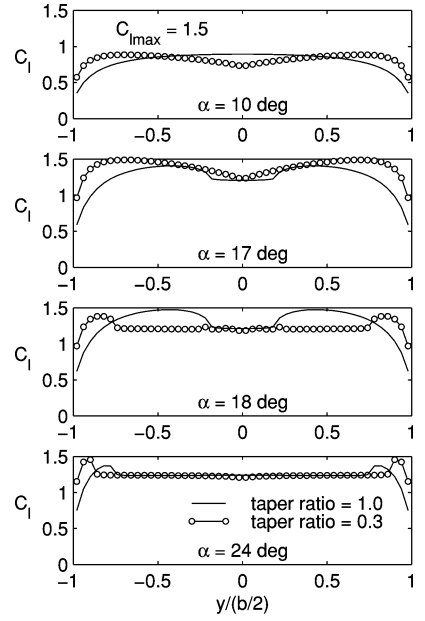

Fig. 14 Spanwise C_l distributions for the rectangular and tapered wings, predicted using VLM3D (scheme 2).

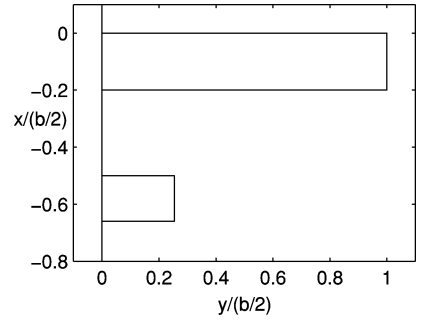

Fig. 15 Planform of the wing-tail configuration.

tapered wing are in accordance with well-known observations from several wind-tunnel and flight-test experiments. The example, therefore, demonstrates the usefulness of the current approach in wing design and analysis for stall and poststall behavior.

Example 3: Wing-Tail Configuration

This example illustrates the effectiveness of the current method for a multiple-lifting-surface configuration. In this example, results are presented for a high-aspect-ratio (AR = 10) constant-chord wing geometry with a conventional aft tail. The planform for the wing-tail configuration is shown in Fig. 15. For this example, a single airfoil is assumed for both the wing and tail. The airfoil lift curve is the hypothetical lift curve shown earlier in Fig. 12.

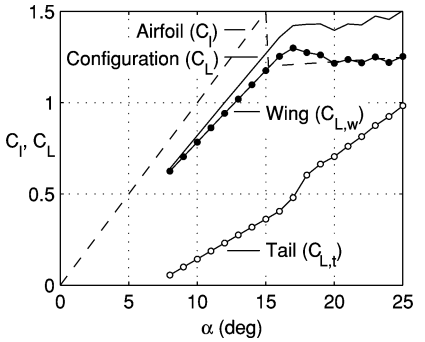

Fig. 16 Lift curves for the airfoil, the wing-tail configuration, and the individual contributions of the wing and the tail.

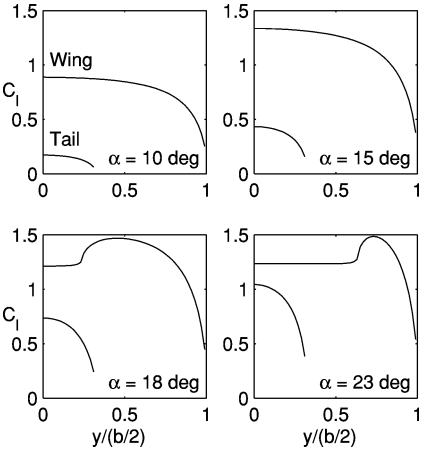

Fig. 17 Spanwise C_l distributions for the wing-tail configuration.

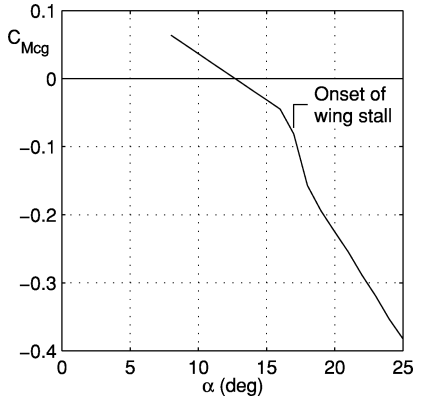

Fig. 18 Pitching-moment curve for the wing-tail configuration.

Figure 16 shows the predicted C_L-α curve for the wing-tail configuration with scheme 2 and starting δ_1 values of -25 deg for all sections at each α. In the same figure, the airfoil C_l-α curve is also plotted for comparison. Figure 16 also shows the $C_{L,w}$ and $C_{L,t}$ as a function of α. The tail $C_{L,t}$ in this plot is nondimensionalized with reference to the tail area. It can be seen that the wing stalls when α just exceeds 17 deg. In this example, the tail remains unstalled over the entire α range considered. The spanwise C_l distributions are shown in Fig. 17 for α values of 10, 15, 18, and 23 deg. These values were chosen for illustrating the stall behavior.

Of particular interest when studying wing-tail configurations is the aircraft pitching moment about the c.g. For this analysis, the c.g. was located to provide a static margin of 10% of the wing mean aerodynamic chord. A tail incidence of -5 deg was chosen so that the aircraft is trimmed at α of 13 deg. In other words, the C_{Mcg} is nearly zero at α of 13 deg. Figure 18 shows the variation of the aircraft C_{Mcg} as a function of α. As the α is increased, a distinct

increase in the nose-down pitching-moment coefficient (negative $C_{M\mathrm{cg}}$) is seen at the onset of stall at α of 17 deg.

To examine the cause of this nose-down pitching moment at stall onset, it is instructive to study the individual contributions of the wing and the tail to the configuration lift curve as shown in Fig. 16. It can be seen that there is a noticeable increase in the tail $C_{L,t}$ at the onset of wing stall at α of 17 deg. This increase in $C_{L,t}$ at stall onset contributes significantly to the increase in the nose-down pitching moment at stall. The origin of the sudden increase in $C_{L,t}$ at stall can in turn be traced to the shape of the wing spanwise lift distribution at the onset of stall. As seen earlier in Fig. 17, the wing stall occurs at the root for α of 17 deg for this example. This loss in lift over the inboard portion of the wing results in a reduction in the downwash at the tail. In addition, it also results in a pair of trailing vortices originating from the outboard ends of the stalled portion of the wing [at $y/(b/2)$ of approximately ± 0.25]. These trailing vortices cause an upwash at the tail. As a consequence of these two factors, there is a distinct increase in the $C_{L,t}$ and a resulting increase in the nose-down pitching moment at the onset of stall.

Thus, as illustrated by this simple example, a method that can predict the poststall characteristics of wing-tail configurations can provide important information for the study of aircraft longitudinal behavior at poststall conditions. These results can be further improved by the addition of models for taking into consideration the wake deformation and the dynamic-pressure loss in the wing wake.

Conclusions

A novel iteration scheme has been developed to implement a decambering approach that accounts for the boundary-layer separation effects on each section of the wings of a multiple-lifting-surface configuration. This numerical approach, when incorporated in an analysis method such as a vortex-lattice code, allows for the computation of poststall aerodynamic characteristics of wings using known section data. Although it is recognized that the surface streamlines are no longer two dimensional at poststall conditions, the current approach aims to provide rapid but approximate solutions for such conditions for use in poststall flight dynamics and simulation studies and in the early stages of configuration design.

A novel feature of the current iteration scheme is in the computation of the residual, which brings to light the existence of multiple solutions at poststall conditions right during the iteration process. In contrast, earlier approaches were able to identify the existence of multiple solutions only as a result of obtaining multiple converged solutions with different initial conditions in the iteration procedure. The current scheme, therefore, brings new insight to the iterative solution of wing flows using known airfoil characteristics.

The results from the new scheme compare fairly well with wind-tunnel poststall data for wings. The results from the current method also agree well with well-known trends in stall patterns. Although the new iteration scheme is significantly more robust than traditional formulations, there are a few angles of attack at which either convergence is not achieved or nonphysical sawtooth oscillations in the C_l distributions are observed in the stalled regions of the wing. Thus, the current approach, like many of the earlier ones, is not always guaranteed to converge to physically realizable poststall solutions for every geometry and airfoil combination. Nevertheless, the current approach has significant potential in providing information for the analysis of aircraft longitudinal stability and control characteristics at poststall conditions.

Acknowledgments

This research effort is supported under Grant NAG-1-01119 from the NASA Langley Research Center. This support and helpful discussions with the technical monitor, SungWan Kim, are gratefully acknowledged.

References

[1]Tani, I., "A Simple Method of Calculating the Induced Velocity of a Monoplane Wing," Aero. Res. Inst., Tokyo Imperial Univ., Rept. 111 (Vol. 9, 3), Japan, Aug. 1934.

[2]Sivells, J. C., and Neely, R. H., "Method for Calculating Wing Characteristics by Lifting-Line Theory Using Nonlinear Section Lift Data," NACA TN 1269, April 1947.

[3]Schairer, R. S., "Unsymmetrical Lift Distributions on a Stalled Monoplane Wing," Ph.D. Dissertation, California Inst. of Technology, Pasadena, CA, Jan. 1939.

[4]Sears, W. R., "Some Recent Developments in Airfoil Theory," *Journal of the Aeronautical Sciences*, Vol. 23, May 1956, pp. 490–499.

[5]Piszkin, S. T., and Levinsky, E. S., "Nonlinear Lifting Line Theory for Predicting Stalling Instabilities on Wings of Moderate Aspect Ratio," General Dynamics Convair Report CASD-NSC-76-001, San Diego, June 1976.

[6]Levinsky, E. S., "Prediction of Aerodynamic Loading," AGARD Conference Proceedings No. 204, Sept. 1976.

[7]Anderson, J. D., Corda, S., and VanWie, D. M., "Numerical Lifting Line Theory Applied to Drooped Leading-Edge Wings Below and Above Stall," *Journal of Aircraft*, Vol. 17, No. 12, 1980, pp. 898–904.

[8]McCormick, B. W., "An Iterative Non-Linear Lifting Line Model for Wings with Unsymmetrical Stall," *SAE Transactions*, 1989, pp. 91–98.

[9]Tseng, J. B., and Lan, C. E., "Calculation of Aerodynamic Characteristics of Airplane Configurations at High Angles of Attack," NASA CR 4182, Oct. 1988.

[10]van Dam, C. P., Kam, J. C. V., and Paris, J. K., "Design-Oriented High-Lift Methodology for General Aviation and Civil Transport Aircraft," *Journal of Aircraft*, Vol. 38, No. 6, 2001, pp. 1076–1084.

[11]Katz, J., and Plotkin, A., *Low-Speed Aerodynamics*, 2nd ed., Cambridge Aerospace Series, Cambridge Univ. Press, Cambridge, England, UK, 2001.

[12]Dula, M., "XFOIL: An Analysis and Design System for Low Reynolds Number Airfoils," *Low Reynolds Number Aerodynamics*, edited by T. J. Mueller, Lecture Notes in Engineering, Vol. 54, Springer-Verlag, New York, 1989, pp. 1–12.

[13]Press, W. H., Teukolsky, S. A., Vetterling, W. T., and Flannery, B. P., *Numerical Recipes in Fortran—The Art of Scientific Computing*, 2nd ed., Cambridge Univ. Press, New York, 1992, pp. 372–375.

[14]Mukherjee, R., Gopalarathnam, A., and Kim, S., "An Iterative Decambering Approach for Post-Stall Prediction of Wing Characteristics Using Known Section Data," AIAA Paper 2003-1097, Jan. 2003.

[15]Ostowari, C., and Naik, D., "Post Stall Studies of Untwisted Varying Aspect Ratio Blades with an NACA 4415 Airfoil Section—Part 1," *Wind Engineering*, Vol. 8, No. 3, 1984, pp. 176–194.